

# WaterClear-GS: Optical-Aware Gaussian Splatting for Underwater Reconstruction and Restoration

Xinrui Zhang, Yufeng Wang, Shuangkang Fang, Zesheng Wang, Dacheng Qi, Wenrui Ding  
 xr\_zhang@buaa.edu.cn, Beihang University

**Abstract**—Underwater 3D reconstruction and appearance restoration are hindered by the complex optical properties of water, such as wavelength-dependent attenuation and scattering. Existing Neural Radiance Fields (NeRF)-based methods struggle with slow rendering speeds and suboptimal color restoration, while 3D Gaussian Splatting (3DGS) inherently lacks the capability to model complex volumetric scattering effects. To address these issues, we introduce WaterClear-GS, the first pure 3DGS-based framework that explicitly integrates underwater optical properties of local attenuation and scattering into Gaussian primitives, eliminating the need for an auxiliary medium network. Our method employs a dual-branch optimization strategy to ensure underwater photometric consistency while naturally recovering water-free appearances. This strategy is enhanced by depth-guided geometry regularization and perception-driven image loss, together with exposure constraints, spatially-adaptive regularization, and physically guided spectral regularization, which collectively enforce local 3D coherence and maintain natural visual perception. Experiments on standard benchmarks and our newly collected dataset demonstrate that WaterClear-GS achieves outstanding performance on both novel view synthesis (NVS) and underwater image restoration (UIR) tasks, while maintaining real-time rendering. The code will be available at this <https://url>.

**Index Terms**—Underwater 3D reconstruction, underwater restoration, novel view synthesis, Gaussian Splatting

## I. INTRODUCTION

UNDERWATER 3D reconstruction presents unique opportunities for marine exploration [1], [2], autonomous underwater navigation [3], [4], and archaeological research [5], [6]. However, the complex optical properties of the underwater environment pose significant challenges. Underwater imaging, in contrast to clear-air environments, suffers from severe degradation due to wavelength-dependent light attenuation and scattering effects caused by water molecules and suspended particles. These phenomena result in pronounced color distortion, diminished contrast, and suppression of fine structural details, as shown in Figure 1. While traditional single-image underwater restoration methods [7], [8], [9], [10], [11], [12] can leverage statistical priors or data-driven learning to mitigate degradation effects, their direct application to underwater 3D scenes inevitably compromises multi-view consistency due to the inherent frame-by-frame processing paradigm.

Neural Radiance Fields (NeRF) [13] has revolutionized 3D scene representation, enabling high-quality rendering from multi-view images. Recent underwater 3D reconstruction methods have sought to integrate the physics-based underwater imaging models into the NeRF framework [14], [15], [16]. However, these approaches encounter several fundamental limitations in underwater scattering scenarios, such as artifacts in

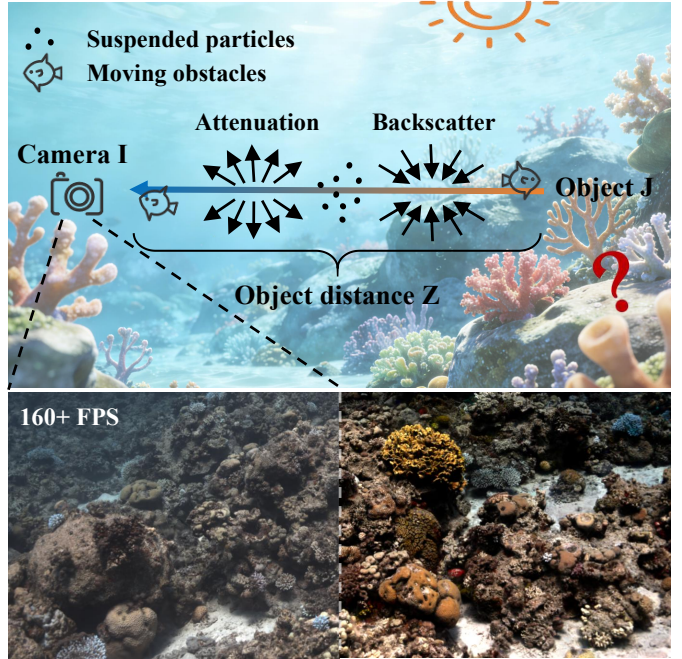


Fig. 1. **Illustration of underwater imaging and our results.** *Top:* Light from objects is affected by significant attenuation and scattering, which intensify with distance. *Bottom:* Our method enables high-quality rendering at over 160 FPS, effectively removes scattering effects, and restores true colors.

volumetric rendering, expensive ray sampling procedures, and slow convergence in underwater scenes due to the additional modeling complexity of water medium effects. To overcome these limitations, recent efforts have transitioned from NeRF to 3D Gaussian Splatting (3DGS) [17], which offers superior rendering efficiency. Pioneering underwater 3DGS variants [18], [19], [20], [21] have attempted to model water medium effects through auxiliary neural networks or volumetric fields. However, these solutions introduce additional shortcomings: (1) compromised training and rendering efficiency of 3DGS, and (2) more critically, suboptimal color restoration quality that ultimately restricts their real-world applicability.

To this end, we present WaterClear-GS, the first underwater 3DGS framework that intrinsically embeds optical physics into Gaussian primitives. Unlike hybrid approaches that patch 3DGS with heavy neural networks, our method introduces a purely explicit optical-aware Gaussian modeling. Each primitive intrinsically encodes the wavelength-specific attenuation and backscatter coefficients, enabling direct learning of underwater optical effects without any auxiliary neural components. We further propose a dual-branch optimization strategy that

simultaneously optimizes underwater and water-free rendering paths, facilitating better color restoration while maintaining geometric consistency. Our method advances the underwater 3D reconstruction by achieving both high-quality geometric reconstruction and realistic color restoration within a unified 3DGS framework, simultaneously addressing computational efficiency for real-time underwater applications.

The main contributions of our work are as follows:

- We propose WaterClear-GS, the first pure explicit 3DGS method that integrates underwater optical-aware modeling into Gaussian primitives, achieving simultaneous underwater scene reconstruction and restoration without relying on separate neural networks for medium.
- We design a dual-branch framework that jointly optimizes underwater 3D reconstruction and water-free color restoration, enhanced by geometry and optics regularization to ensure physical plausibility and visual quality.
- We introduce a new underwater dataset, ShipWreck, featuring complex shipwreck scenes to provide a more challenging and diverse test case than current coral scenes.
- Experiments demonstrate that the proposed WaterClear-GS achieves state-of-the-art results in both NVS and UIR tasks while maintaining real-time rendering capabilities.

## II. RELATED WORK

### A. Novel View Synthesis

Novel view synthesis (NVS) aims to render photorealistic images from arbitrary unseen viewpoints given a set of posed input images. A major breakthrough was introduced by NeRF [13], which represents scenes as a continuous volumetric function parameterized by a multi-layer perceptron (MLP). Colors and densities are predicted by querying the MLP at sampled points along camera rays and integrated via volumetric rendering. Numerous NeRF variants have improved efficiency, quality, or generalization [22], [23], [24], [25], [26], [27], [28], [29], [30], [31]. Examples include fast training through tensor decomposition [23], sparse voxel grids [24], multi-resolution hash grids [22], and factorized scene representations [28], [32]. Other methods address dynamic scenes [33], [34], [35] or large-scale environments [36], [37].

Recently, 3D Gaussian Splatting [17] has emerged as a compelling alternative to NeRF-based approaches. It represents the scene using a set of explicit 3D Gaussians with learnable properties such as position, color, scale, and opacity, achieving state-of-the-art rendering quality while enabling real-time performance. Subsequent works have expanded its applicability to various challenging domains, including sparse-view reconstruction [38], [39], [40], [41], dynamic or deformable scenes [42], [43], and large-scale environments [44], [45], [46], [47]. Further extensions improve shading and appearance modeling [48], [49] or geometric accuracy [50], [51].

### B. Underwater Scene Representation and Restoration

Underwater images suffer from severe degradation caused by wavelength-dependent attenuation and scattering, presenting great challenges to vision tasks. Traditional single-image

methods [52], [8], [7], [53] typically rely on hand-crafted priors, such as the dark channel or white balance assumptions, but these priors break down under strong color casts or spatially varying illumination in underwater environments. Akkaynak and Treibitz [54] introduced the revised underwater image formation model, which separates direct transmission from backscatter and explicitly accounts for wavelength-dependent attenuation, forming the foundation of many subsequent methods. Although extensive progress has been made in single-image underwater enhancement and restoration [9], [10], [55], [11], [12], they inevitably introduce inconsistencies when applied independently to each view in 3D scenes. This limitation highlights the need for underwater scene modeling approaches that jointly reason about the imaging physics and 3D structure.

With the rise of neural rendering, several recent works [16], [15], [56], [57], [14], [18], [19], [20], [21] attempt to incorporate underwater physics into NeRF or 3DGS for multi-view reconstruction. WaterNeRF [56] jointly estimates scene density, color, and attenuation parameters within the NeRF framework. WaterHE-NeRF [57] predicts illuminance attenuation alongside radiance and takes the histogram-equalized image as a pseudo GT value to guide color restoration. SeaThru-NeRF [14] explicitly models scattering media and decomposes the rendering process into direct and backscatter components. However, these NeRF-based methods generally suffer from high training costs and often yield suboptimal reconstruction quality. WaterSplatting [18] extends 3DGS by representing the water medium as an additional volumetric field, while SeaSplat [19] predicts attenuation and scattering maps using two separate learned medium models. Aquatic-GS [20] introduces neural water fields that predict medium parameters conditioned on viewpoint. RestorGS [21] employs an additional color MLP and a CNN to predict color mapping and illumination map, respectively, though it increases architectural complexity.

Although these approaches improve underwater reconstruction, most rely on implicit networks or additional volumetric fields to estimate medium properties. Due to the difficulty of consistently estimating per-view medium parameters, they often incur higher memory usage, unstable optimization behavior, and limited color restoration accuracy. Moreover, modeling the water medium as a separate component often complicates the rendering pipeline and reduces runtime efficiency. In contrast, our method directly embeds wavelength-dependent medium properties into the Gaussian primitives themselves, enabling the rendering pipeline to operate entirely within a unified, CUDA-efficient 3DGS framework. This eliminates the need for separate implicit fields or additional MLP estimators, resulting in faster convergence, real-time rendering performance, and significantly improved color fidelity in underwater reconstruction and restoration.

## III. METHODOLOGY

### A. Preliminaries

1) *3D Gaussian Splatting*: 3DGS represents a scene using a large number of anisotropic 3D Gaussian primitives, each defined by a center  $\mu \in \mathbb{R}^3$ , a covariance matrix  $\Sigma$ , an

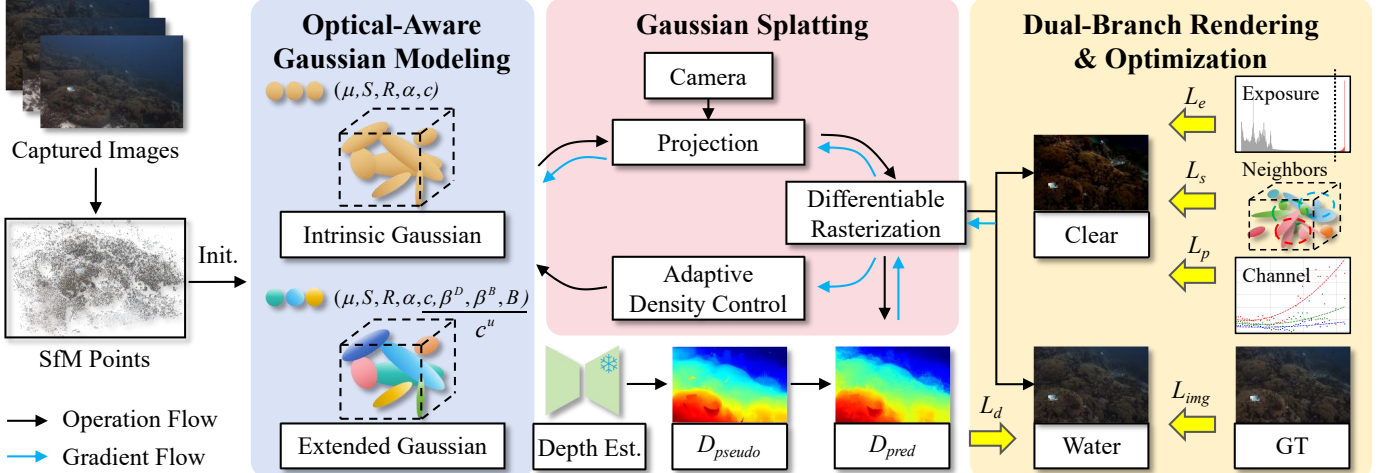


Fig. 2. **Overview of the WaterClear-GS framework.** Our method extends each Gaussian with water optical parameters  $\beta^D$ ,  $\beta^B$  and  $B$ . The dual-branch design simultaneously renders underwater images by applying these parameters and clear images by zeroing them out. Depth-guided enhancement guides the geometry optimization, while exposure constraint balances the dynamic range of restored color and spatially-adaptive regularization, together with spectral regularization, ensures physical plausibility of medium properties. Our framework ensures high-quality reconstruction and realistic color restoration.

opacity  $\alpha \in [0, 1]$ , and a set of spherical harmonic (SH) coefficients  $C \in \mathbb{R}^k$  for modeling view-dependent appearance. The Gaussian density is given by:

$$\mathcal{G}(\mathbf{x}) = \exp\left(-\frac{1}{2}(\mathbf{x} - \boldsymbol{\mu})^T \boldsymbol{\Sigma}^{-1}(\mathbf{x} - \boldsymbol{\mu})\right). \quad (1)$$

The covariance matrix  $\boldsymbol{\Sigma}$  is decomposed into a scaling matrix  $S$  (represented by a vector  $s \in \mathbb{R}^3$ ), and a rotation matrix (derived from a quaternion  $q \in \mathbb{R}^4$ ) as:

$$\boldsymbol{\Sigma} = RSS^T R^T. \quad (2)$$

During rendering, each 3D Gaussian is projected to a 2D ellipse on the image plane, and only the Gaussians overlapping a pixel contribute to its color. The final color is accumulated through  $\alpha$ -blending:

$$C = \sum_{i=1}^N c_i \alpha_i \prod_{j < i} (1 - \alpha_j), \quad (3)$$

where  $N$  is the number of Gaussians, and the depth is rendered using the same transmittance weights:

$$D = \sum_{i=1}^N z_i \alpha_i \prod_{j < i} (1 - \alpha_j). \quad (4)$$

Through iterative optimization with photometric supervision and adaptive density control which clones, splits, or prunes Gaussians based on gradient magnitude, the model progressively refines the number of Gaussians and their attributes until they can effectively represent the entire 3D scene.

2) *Underwater Image Formation Model:* Unlike imaging in clear air, image formation in scattering media is affected by the medium in two aspects. On one hand, the signal reflected from objects undergoes distance- and wavelength-dependent attenuation as it propagates through the medium. On the other hand, the in-scattering of ambient light by suspended particles introduces a view-dependent backscatter component along the line of sight (LOS). This backscatter is independent

of scene content but accumulates with distance, reducing visibility and contrast while causing severe color distortion. Following the revised underwater imaging model of Akkaynak and Treibitz [54], the image  $I$  captured at distance  $z$  can be expressed as:

$$I = \underbrace{J \cdot e^{-\beta^D(\mathbf{v}_D)z}}_{\text{direct component}} + \underbrace{B^\infty \cdot (1 - e^{-\beta^B(\mathbf{v}_B)z})}_{\text{backscatter component}}, \quad (5)$$

where  $J$  is the true radiance of the object, and  $\beta^D(\mathbf{v}_D)$  and  $\beta^B(\mathbf{v}_B)$  denote the wavelength-dependent attenuation and backscatter coefficients. The vectors  $\mathbf{v}_D$  and  $\mathbf{v}_B$  encode the dependence of the coefficients on multiple wavelength-related factors, including object reflectance, ambient illumination, water-body scattering properties, and the camera's spectral response. Both terms are inherently channel-dependent, explaining the nonlinear interaction between distance, wavelength, and color distortion observed in underwater images. The backscatter term  $B^\infty$  represents the water color from backscattering at infinity (also called veiling light or ambient light), which is typically non-uniform due to the directionality of sunlight and other factors [58].

## B. WaterClear-GS Overview

WaterClear-GS is built upon 3DGS framework but extends it with a physically grounded formulation tailored for underwater imaging. As illustrated in Figure 2, WaterClear-GS augments each Gaussian primitive with wavelength-dependent attenuation, backscatter, and veiling light parameters, enabling the representation itself to capture local water-medium effects without relying on an auxiliary implicit network. To jointly achieve accurate underwater reconstruction and faithful color restoration, we introduce a dual-branch rendering strategy that synthesizes both underwater and water-free views from the same set of Gaussians, enforcing geometric consistency while progressively recovering true object appearance. This

section introduces our optical-aware Gaussian modeling approach, followed by the dual-branch optimization strategy and regularization mechanisms.

1) *Optical-Aware Gaussian Modeling*: To enable Gaussian primitives to inherently model underwater attenuation and backscatter, we associate each Gaussian with local, wavelength-dependent optical parameters and apply them to modulate its color before rasterization. For the  $i$ -th Gaussian, let  $c_i^o \in \mathbb{R}^3$  be the original color predicted from spherical harmonics (SH), and let  $d_i = (\mu_i - c)_z$  denote the distance from the camera center  $c$ . We define channel-wise direct attenuation, backscatter, and veiling-light coefficients  $\beta_i^D, \beta_i^B, B_i \in \mathbb{R}^3$ , and compute the underwater-corrected color as:

$$c_i^u = T_i^D \cdot c_i^o + (1 - T_i^B) \cdot B_i, \quad (6)$$

where  $T_i^D = \exp(-\beta_i^D d_i)$  and  $T_i^B = \exp(-\beta_i^B d_i)$  are wavelength-dependent transmittances applied element-wise over RGB. During  $\alpha$ -blending, the underwater color  $c_i^u$  simply replaces the original SH-predicted color  $c_i^o$ , yielding the rendered pixel:

$$C^u = \sum_{i=1}^N c_i^u \alpha_i \prod_{j < i} (1 - \alpha_j). \quad (7)$$

The optical parameters  $\beta_i^D, \beta_i^B, B_i$  are fully differentiable and optimized jointly with all other Gaussian attributes. Assigning these parameters at the primitive level enables the model to capture spatially varying water-body properties, avoiding the computational overhead and inaccuracies of auxiliary MLPs while encouraging convergence toward physically consistent attenuation–scattering behavior.

2) *Dual-Branch Optimization Strategy*: To enable both faithful underwater reconstruction and accurate color recovery, we design a dual-branch optimization strategy that jointly supervises the scene under two rendering conditions: *water* and *clear*. The *water* branch renders images using the full underwater formation model. By fitting the input underwater images, this branch provides geometric supervision and constrains the learned attenuation and backscatter parameters to be consistent with real observations. The *clear* branch renders the same Gaussian primitives after removing all water-medium terms, effectively simulating an ideal water-free environment. This branch encourages the model to recover intrinsic object colors that are not directly available from supervision. Crucially, it acts as a regularization that forces the disentanglement of scene appearance from water effects, preventing degenerate solutions where the model might incorrectly attribute scattering effects to the object’s surface texture. Sharing the same set of Gaussian primitives, the two rendering branches collaboratively optimize the representation, acting as mutual constraints and facilitators to achieve a balanced result.

### C. Optimization for Reconstruction

1) *Depth-Guided Geometric Regularization*: In underwater imaging, depth information plays a crucial role in accurately modeling scene geometry. The effects of light attenuation and scattering, governed by the learned optical parameters, are exponentially dependent on the propagation distance. Moreover,

conventional Gaussian-based 3D representations often suffer from floating artifacts and geometric instability, especially in water bodies where texture cues are weak and depth ambiguity is severe. To address this, we introduce a depth-guided geometric regularization mechanism to stabilize the 3D representation learning.

We leverage the powerful monocular depth estimation model DepthAnythingV2 [59] to generate pseudo-depth maps. Typical pixel-wise L1 losses on depth map may lead to scale and shift ambiguities. To alleviate this issue and emphasize structural consistency rather than absolute depth values, we employ a Pearson correlation coefficient (PCC) based loss to maximize the similarity between the predicted depth  $D_{pred}$  and the pseudo-depth  $D_{pseudo}$ :

$$L_d = 1 - \frac{\text{Cov}(D_{pred}, D_{pseudo})}{\sigma(D_{pred}) \sigma(D_{pseudo})}. \quad (8)$$

This correlation-based formulation focuses on the relative depth relationships across the scene. Since our goal is to leverage the robust 2D structural priors from the foundation model to guide 3D geometry rather than distilling absolute metric depth, this scale-invariant loss effectively prevents the propagation of scale/shift errors from the monocular estimator.

2) *Perception-Driven Image Loss*: Underwater scenes exhibit strong wavelength-dependent attenuation and scattering, resulting in highly unbalanced illumination and color-dependent degradation. Conventional image loss used by 3DGS treats all pixels uniformly, causing optimization to be dominated by bright regions while neglecting low-intensity areas. This leads to a visually imbalanced reconstruction, where foreground objects are rendered with relatively high fidelity, but background scenes and shadowed areas suffer from blurring, distortion, or a complete loss of detail.

Inspired by RawNeRF [60], we perform a perception-driven transformation  $\psi(\cdot)$  that adaptively rescales image intensities to balance gradient magnitudes across illumination levels. Define a gradient supervised mapping on the estimated image  $\hat{y}$  and the ground truth image  $y$ :

$$\psi(y) = \frac{y}{\text{sg}(\hat{y}) + \epsilon}, \quad (9)$$

where  $\epsilon=10^{-3}$  ensures numerical stability and  $\text{sg}(\cdot)$  denotes the stop-gradient operator. Using  $\text{sg}(\hat{y})$  rather than  $\text{sg}(y)$  allows the model to adaptively emphasize different regions based on its own predictions. This transformation  $\psi(\cdot)$  behaves like a differentiable inverse-intensity tone mapping that redistributes gradient energy across the dynamic range, ensuring that darker regions receive sufficient supervision while maintaining numerical stability in bright areas.

The photometric reconstruction loss is evaluated in the perceptual domain:

$$\mathcal{L}_{W-L2} = \frac{1}{N} \|\psi(\hat{y}) - \psi(y)\|_2^2, \quad (10)$$

where  $N$  denotes the total number of pixels. Similarly, the structural similarity loss is computed between the transformed images:

$$\mathcal{L}_{W-DSSIM} = 1 - \text{SSIM}(\psi(\hat{y}), \psi(y)), \quad (11)$$

which effectively measures perceptual similarity in a tone-mapped domain, enhancing sensitivity to structural errors in low-intensity regions. Then the final image reconstruction loss combines the two terms:

$$\mathcal{L}_{\text{img}} = (1 - \lambda_{\text{SSIM}}) \mathcal{L}_{\text{W-L2}} + \lambda_{\text{SSIM}} \mathcal{L}_{\text{W-DSSIM}}. \quad (12)$$

#### D. Optimization for Restoration

The absence of ground-truth supervision introduces inherent ambiguity between the recovered colors and the estimated attenuation–scattering parameters, leading to multiple visually plausible but physically inconsistent solutions. To constrain the solution space, we employ three complementary components: an exposure constraint to avoid over-amplification of highlights, a spatially-adaptive regularization to stabilize neighboring Gaussians, and a physically guided spectral prior to enforce wavelength-consistent ordering of the optical coefficients.

1) *Exposure Constraint*: Underwater scenes often contain uneven illumination, and the interplay between attenuation estimation and color recovery can make the restored results susceptible to overexposure. This issue is further amplified by the perception-driven reconstruction loss, which up-weights dark regions and may inadvertently encourage the network to brighten the output to reduce the weighted error. To maintain a visually natural dynamic range consistent with human perception, we introduce an exposure regularization term that penalizes over-bright regions in the restored image:

$$\mathcal{L}_e = \frac{1}{|\Omega|} \sum_{p \in \Omega} \left\{ \max(I_{\text{clear}}(p) - \tau, 0) \right\}, \quad (13)$$

where  $I_{\text{clear}}$  represents the water-free rendered image,  $\Omega$  denotes the set of image pixels,  $\tau$  represent the brightness thresholds. This constraint prevents overexposure and encourages balanced illumination across the restored scene.

2) *Spatially-Adaptive Regularization*: To model more plausible non-uniform optical properties in underwater environments, we propose a spatially-adaptive regularization method based on local consistency. This approach applies distance-weighted neighborhood smoothing constraints to key water optical parameters ( $\beta^D$ ,  $\beta^B$ ,  $B$ ). Specifically, for each visible Gaussian from the current viewpoint, we perform local smoothing within a spherical neighborhood of radius  $r$ , constraining parameter consistency with neighboring Gaussians through the following loss function:

$$L_s = \frac{1}{|V|} \sum_{i \in V} \frac{\sum_{j \in \mathcal{N}_i} \|\theta_i - \theta_j\|_2^2 \cdot w_{ij}}{\sum_{j \in \mathcal{N}_i} w_{ij}}, \quad (14)$$

where  $V$  represents the set of valid Gaussians with sufficient neighbors ( $\geq n_{\text{min}}$ ),  $\mathcal{N}_i$  denotes the neighborhood of Gaussian  $i$ ,  $\theta$  represents the water optical parameters to be smoothed, and  $w_{ij} = 1/(d_{ij} + \varepsilon)$  is a weight based on the Euclidean distance  $d_{ij}$ . This distance-weighted local smoothing mechanism only requires local consistency rather than global uniformity, preserving the ability of optical parameters to vary with depth and water quality.

3) *Physically Guided Spectral Regularization*: To encode physically plausible spectral behavior of underwater light propagation, we introduce a lightweight physics-inspired regularizer that enforces soft spectral ordering across RGB wavelengths among the learned per-Gaussian optical parameters.

For each Gaussian, the optical parameters are wavelength-dependent: the attenuation  $\beta^D(i) = [\beta_r^D, \beta_g^D, \beta_b^D]_i$ , the backscatter  $\beta^B(i) = [\beta_r^B, \beta_g^B, \beta_b^B]_i$ , and the veiling light  $B(i) = [B_r, B_g, B_b]_i$  are each defined with separate values at red, green, and blue wavelengths. We define their combined spectral differences as:

$$\Delta_i = [\Delta\beta^D(i), \Delta\beta^B(i), \Delta B(i)], \quad (15)$$

$$\begin{cases} \Delta\beta^D(i) = [\beta_g^D(i) - \beta_r^D(i), \beta_b^D(i) - \beta_g^D(i)], \\ \Delta\beta^B(i) = [\beta_r^B(i) - \beta_g^B(i), \beta_g^B(i) - \beta_b^B(i)], \\ \Delta B(i) = [B_r(i) - B_g(i), B_g(i) - B_b(i)]. \end{cases} \quad (16)$$

The physical prior loss softly penalizes violations of the expected spectral ordering using a smooth *Softplus* function:

$$L_p = \mathbb{E}_i [\text{Softplus}(\Delta_i + \delta)], \quad (17)$$

where  $\delta$  is a small tolerance margin. It softly enforces the underwater spectral priors: red attenuates fastest, blue scatters most, and bluish veiling light, while remaining continuous and differentiable, which stabilizes training and avoids gradient discontinuities at spectral boundaries.

The total loss function for the WaterClear-GS is defined as:

$$L_{\text{total}} = L_{\text{img}} + \lambda_d L_d + \lambda_s L_s + \lambda_p L_p + \lambda_e L_e. \quad (18)$$

## IV. EXPERIMENTS

### A. Experimental Setup

1) *Public Datasets*: SeaThru-NeRF [14] is a real-world underwater dataset captured by a Nikon D850 SLR camera, including Panama, Curasao, IUI3-RedSea and JapaneseGardens-RedSea. We also employ the D3 and D5 datasets from SeaThru [61], captured by a Sony α7R Mk III camera and a Nikon D810 camera, respectively. Each dataset is divided into training and testing subsets as follows: Panama (15/3), Curasao (18/3), JapaneseGardens-RedSea (17/3), IUI3-RedSea (25/4), D3 (59/9), and D5 (37/6). All images are captured under natural underwater illumination. For D3 and D5, we apply gamma correction to the original linear-space PNGs following SeaThru [61]. The Curasao, D3 and D5 scenes contain complete and visible color charts, making them suitable for evaluating image color restoration performance.

2) *Self-Collected Dataset*: Noticing the limitations of existing datasets in terms of scene diversity, we construct a new challenging real-world underwater dataset named ShipWreck. Images are collected from publicly available online videos, which contain two shipwreck scenes with complex structures, metal surfaces, and varying water conditions. Each scene includes high-resolution images (1920×1080) captured from diverse viewpoints, with 90 and 36 images, respectively. Training and testing subsets are divided as: ShipWreck-1 (78/12), ShipWreck-2 (31/5). Camera intrinsics and poses are estimated using COLMAP [62] for initialization.

TABLE I

QUANTITATIVE RESULTS OF THE NVS TASK ON THE SEATHRU-NERF DATASET. HIGHLIGHTS THE TOP THREE: FIRST, SECOND, AND THIRD.

Method	Panama			Curaçao			IUI3-RedSea			J.G.-RedSea			Avg. Time↓	Avg. FPS↑
	PSNR↑	SSIM↑	LPIPS↓	PSNR↑	SSIM↑	LPIPS↓	PSNR↑	SSIM↑	LPIPS↓	PSNR↑	SSIM↑	LPIPS↓		
3DGS [17]	29.59	0.919	0.181	30.92	0.936	0.183	24.26	0.896	0.245	22.08	0.851	0.207	3.6min	241.14
STN [14]	27.82	0.838	0.266	30.29	0.881	0.251	25.97	0.787	0.316	21.78	0.769	0.294	10.5h	0.13
Seasplat [19]	29.86	0.935	0.147	29.82	0.925	0.165	28.43	0.900	0.220	23.24	0.874	0.180	29.8min	50.55
WS [18]	31.64	0.943	0.104	32.67	0.950	0.140	29.76	0.909	0.203	24.20	0.896	0.136	9.5min	73.28
Ours	32.27	0.950	0.112	33.49	0.956	0.136	30.04	0.916	0.200	24.35	0.900	0.147	15.7min	160.48

TABLE II

QUANTITATIVE COMPARISON OF THE NVS TASK ON THE SEATHRU DATASET. HIGHLIGHTS THE TOP THREE: FIRST, SECOND, AND THIRD.

Method	D3			D5			Avg. Time↓	Avg. FPS↑
	PSNR↑	SSIM↑	LPIPS↓	PSNR↑	SSIM↑	LPIPS↓		
3DGS [17]	27.99	0.844	0.289	29.94	0.903	0.281	3.5min	228.67
STN [14]	20.34	0.562	0.555	24.34	0.801	0.453	10h	0.12
Seasplat [19]	28.27	0.851	0.256	28.98	0.904	0.263	27.3min	67.35
WS [18]	28.03	0.852	0.219	30.62	0.910	0.247	13min	76.14
Ours	28.48	0.860	0.214	30.79	0.919	0.245	16.7min	176.63

TABLE III

QUANTITATIVE COMPARISON OF THE NVS TASK ON THE SHIPWRECK DATASET. HIGHLIGHTS THE TOP THREE: FIRST, SECOND, AND THIRD.

Method	ShipWreck-1			ShipWreck-2			Avg. Time↓	Avg. FPS↑
	PSNR↑	SSIM↑	LPIPS↓	PSNR↑	SSIM↑	LPIPS↓		
3DGS [17]	27.39	0.852	0.196	24.80	0.855	0.191	8.6min	191.57
STN [14]	20.00	0.530	0.580	24.01	0.767	0.315	12h	0.10
Seasplat [19]	27.62	0.853	c0.187	25.18	0.863	0.189	33.8min	61.12
WS [18]	26.74	0.840	0.191	24.34	0.852	0.187	12.5min	78.35
Ours	27.71	0.858	0.177	25.31	0.865	0.182	13.5min	160.16

3) *Baselines*: On the task of NVS, we compare our method with vanilla 3DGS [17] and several state-of-the-art underwater methods: 1) NeRF-based methods, SeaThru-NeRF (STN) [14]; and 2) 3DGS-based methods, including WaterSplatting (WS) [18] and SeaSplat [19]. On the task of UIR, we only compare ours with these underwater methods.

4) *Metrics*: For the NVS task, we evaluate the Peak Signal-to-Noise Ratio (PSNR), Structural Similarity Index Measure (SSIM) [63], and Learned Perceptual Image Patch Similarity (LPIPS) [64] between the rendered and ground-truth underwater images on the test datasets. We also report the training time and rendering FPS to evaluate model efficiency. For the UIR task, obtaining ground-truth references is challenging. Following prior underwater enhancement studies [58], [65], [66], we adopt the CIEDE2000 color difference ( $\Delta E_{00}$ ) [67] and the average angular error  $\bar{\psi}$  (in degrees) [68] to assess color restoration quality on datasets containing standard color charts.  $\Delta E_{00}$  quantifies perceptual color differences in the CIELAB color space, which is derived from RGB through a perceptually uniform nonlinear transformation.  $\bar{\psi}$  measures color accuracy as the angle between restored and reference color vectors in RGB space. It is computed over 12 color chart patches to assess restoration fidelity in our experiments.

5) *Implementation Details*: Our method is based on the pipeline of 3DGS method. Each dataset is trained for 15,000 iterations. Densification strategy is adjusted to perform every

500 iterations. For the image reconstruction loss,  $\lambda_{SSIM} = 0.2$ . For the depth-guided PCC loss,  $\lambda_d$  is set to 0.2. For exposure constraint  $L_e$ , the exposure threshold  $\tau$  is set to 0.9, with corresponding weights  $\lambda_e = 0.1$ . Spatial regularization  $L_s$  and physical prior regularization  $L_p$  are performed every 10 iterations.  $\lambda_s$  and  $\lambda_p$  are set to 0.1 and smooth radius is set to 0.05 with at least 2 neighbors. Owing to the wavelength-dependent attenuation and scattering properties of the water medium, the parameters  $\beta_D$ ,  $\beta_B$  and  $B$  are each modeled as three-component vectors that correspond to the RGB channels. The learning rates are set to 0.0001 for  $\beta_D$  and  $\beta_B$ , and 0.001 for  $B$ . We do not employ additional spherical-harmonics (SH) coefficients; only RGB values are used as the base color representation for each Gaussian. All experiments are conducted on a single NVIDIA RTX 4090 GPU.

### B. Novel View Synthesis Results

We first report the quantitative results on the NVS task in Table I, Table II and Table III. The results demonstrate that our method consistently achieves superior performance, attaining the highest PSNR and SSIM across all datasets, despite slightly suboptimal LPIPS scores in a few cases. While WaterSplatting benefits from the inherent smoothness of volumetric fields, our Gaussian-based representations preserve sharper appearance boundaries and color transitions, which LPIPS tends to penalize. Notably, our approach strikes a favorable balance between quality and efficiency. While NeRF-based underwater models SeaThru-NeRF require hours of training per scene, and 3DGS variants augmented with additional medium networks (e.g., WaterSplatting) incur noticeable overhead, our method retains the highest FPS advantage of the 3DGS pipeline. Specifically, WaterClear-GS achieves over 160 FPS on average, which is 2 $\times$  faster than WaterSplatting and Seasplat, and orders of magnitude faster than SeaThru-NeRF. This efficiency stems from embedding underwater optical effects directly into Gaussian rendering without auxiliary volumetric fields or MLP estimators. This means that our method can support more real-time applications.

Figure 3 presents qualitative comparisons of the NVS results. On the SeaThru-NeRF dataset, 3DGS exhibits severe artifacts and blurred distant structures, as the original formulation does not account for medium and thus struggles under strong degradation. For the D3 and D5 scenes with lower exposure and more turbid water conditions, SeaThru-NeRF fails to reconstruct valid geometry, resulting in incomplete structures and heavily distorted colors. Seasplat performs more robustly overall, yet still produces localized distortions, such

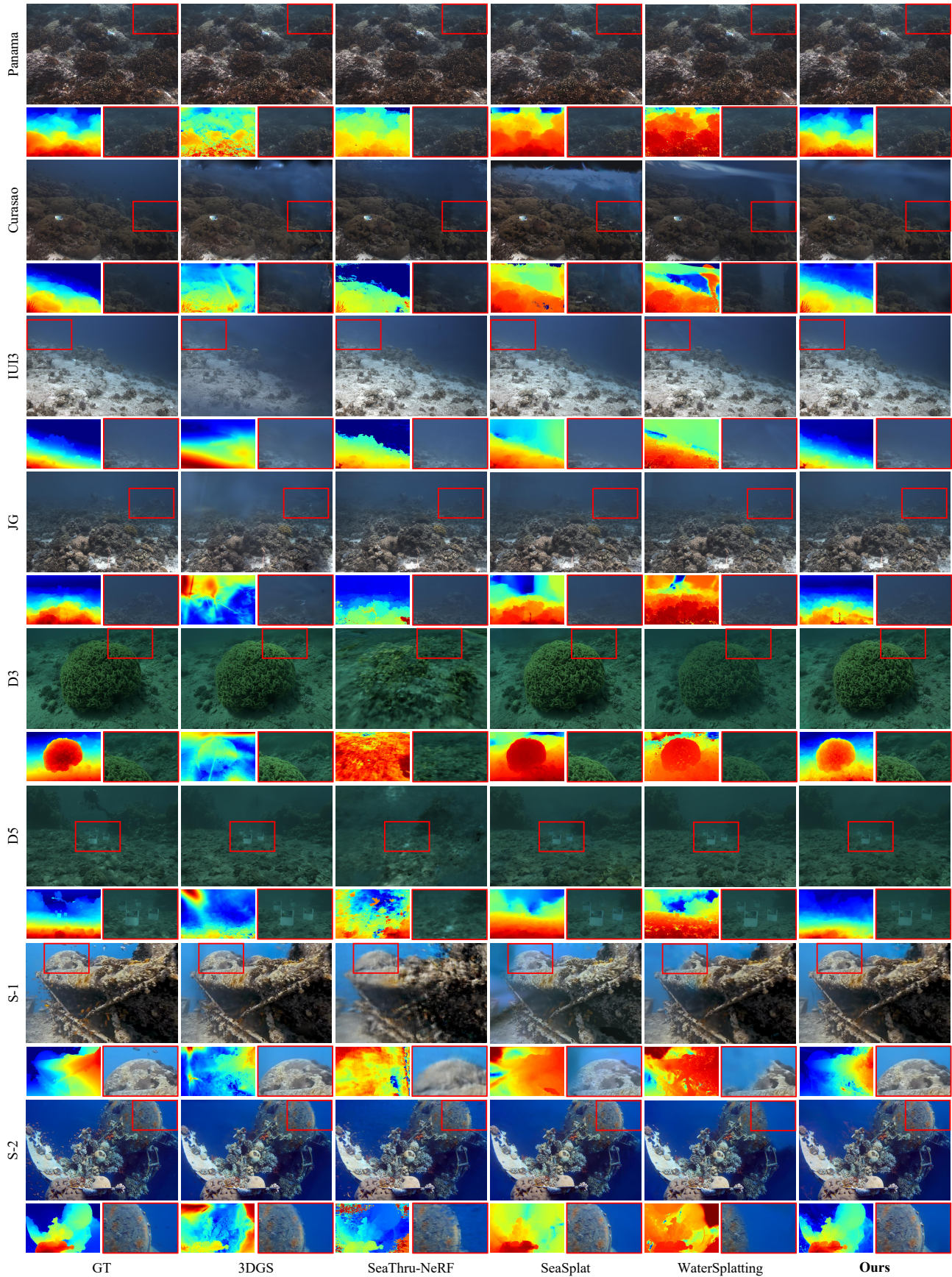


Fig. 3. **Qualitative results of the NVS task.** We present rendered underwater images and their depth maps. The pseudo-depth maps are used as a reference. Zoomed-in regions (highlighted with red bounding boxes) illustrate detailed differences. Our method consistently preserves geometric structures and fine-level details in most cases.



Fig. 4. **Qualitative results of the UIR task.** Details are zoomed in and highlighted with red and yellow bounding boxes. In contrast to other methods, which often produce grayish, underexposed, or severely color-shifted results, our method restores images with more natural visual quality.

TABLE IV  
QUANTITATIVE RESULTS OF THE UIR TASK. HIGHLIGHTS THE TOP TWO  
IN EACH METRIC: FIRST AND SECOND.

Scene Method	Curasao		D3		D5	
	$\Delta E_{00} \downarrow$	$\bar{\psi} \downarrow$	$\Delta E_{00} \downarrow$	$\bar{\psi} \downarrow$	$\Delta E_{00} \downarrow$	$\bar{\psi} \downarrow$
STN [14]	16.67	19.77	40.89	32.54	40.76	31.42
Seasplat [19]	15.78	18.61	27.98	27.53	41.37	27.06
WS [18]	19.98	22.98	30.82	28.09	36.09	25.76
<b>Ours</b>	12.67	10.71	27.82	27.20	30.37	24.87

as inconsistent textures in the Curasao, J.G.-RedSea, and ShipWreck-1 scenes. WaterSplatting achieves sharper details but occasionally misattributes water-medium effects to object surfaces, leading to incorrect occlusions and unnatural color biases, particularly visible in the D5 and ShipWreck datasets. Depth maps further reveal the shortcomings of existing methods. Under the influence of water medium and ambiguous attenuation, these methods tend to inject floating artifacts or irregular blobs near the camera to compensate for depth uncertainty, degrading both geometry and appearance. In contrast, WaterClear-GS produces more accurate depth distributions and preserves fine-grained structural details, owing to its optical modeling and geometry-aware regularization. As a result, our method delivers more robust and visually consistent reconstructions with cleaner boundaries and more reliable depth maps across diverse underwater conditions.

### C. Underwater Images Restoration Results

Figure 4 shows the qualitative comparison of underwater image restoration. SeaThru-NeRF often fails to reconstruct several scenes due to strong degradation and insufficient multi-view constraints; even when reconstruction succeeds, the restored images show only marginal improvements with limited recovery of color and details. Seasplat produces visually enhanced outputs but frequently introduces unnatural color shifts and oversaturated regions, particularly in the D5 and ShipWreck-1 scenes. WaterSplatting also tends to generate outputs with noticeably reduced brightness and produces hazy, low-contrast renderings across all datasets, largely because it overestimates the contribution of scattering medium. In contrast, WaterClear-GS yields visually compelling restorations with natural color saturation, enhanced contrast, and sharper fine-scale structures. Thanks to the wavelength-dependent optical modeling embedded in each Gaussian, our method restores color tones—especially in the severely attenuated red channel—more faithfully than competing approaches. This leads to restorations that better align with human visual perception and more accurately reflect the true appearance of underwater scenes.

To quantitatively evaluate the color restoration quality of each model, we compute the color difference  $\Delta E_{00}$  and the average angular error  $\bar{\psi}$  (in degrees) between the restored and ground-truth colors on three scenes that include complete standard color charts. As reported in Table IV, our method consistently achieves the best performance, with the lowest  $\Delta E_{00}$  and  $\bar{\psi}$  across all scenes. On the Curasao scene, our approach attains the lowest  $\Delta E_{00}$  and  $\bar{\psi}$ , improving over the

second-best method by 3.11 and 7.90, respectively. A similar advantage is observed on the D5 scene, where our method ranks first on both metrics and maintains a clear margin over competing approaches. These results demonstrate that WaterClear-GS not only minimizes perceptual color error but also preserves chromatic angular consistency more accurately, leading to faithful and stable restoration under a wide range of underwater degradation conditions.

### D. Analysis on the Optical-Aware Gaussian Modeling

1) *Physical Interpretation:* We visualize the learned attenuation  $\beta_D$ , backscatter  $\beta_B$ , and veiling light  $B$  across all Gaussians as Figure 5a, 5b, and 5c. These parameters exhibit clear physical structure: all RGB channels follow the expected spectral ordering ( $\beta_r^D > \beta_g^D > \beta_b^D$ ,  $\beta_b^B > \beta_g^B > \beta_r^B$ ,  $B_b > B_g > B_r$ ), confirming the interpretability of our optical-aware formulation. Importantly, these parameters are defined per Gaussian and represent the local optical properties of the water medium; they are therefore not inherently functions of the camera–point distance. The effect of distance is already handled by the rendering equation through the exponential transmission terms. Nevertheless, when plotting the learned parameters against depth, smooth depth-related trends emerge:  $\beta^D$  tends to increase with distance, while  $\beta^B$  and  $B$  rise in mid-range regions and decrease for very distant Gaussians. Note that the depth-related trends observed are not inherent distance-dependent definitions, but dataset-driven correlations that naturally emerge in forward-facing underwater captures, where distant regions typically exhibit stronger attenuation, backscatter, and ambient veiling. But in surround capture setups, such depth-related patterns may weaken or disappear.

2) *Effect of Multichannel Optical Parameters:* To further validate the necessity of modeling wavelength-dependent optical effects, we replace the three-channel optical parameters  $\beta^D, \beta^B, B \in \mathbb{R}^3$  with single-channel scalars shared across RGB. As shown in Figure 6, this modification leads to noticeable hue shifts in restored images. And distant regions become unrealistically blue due to the inability to attenuate short-wavelength components relative to red and green. This confirms that single-channel optical modeling fails to capture the spectral behavior of underwater light propagation. This experiment highlights that multichannel optical modeling is essential for accurate color restoration, particularly for recovering long-wavelength components.

3) *Impact of Color Representation:* In contrast to in-air scenes where high-order spherical harmonics (SHs) are essential for modeling view-dependent specularities, the underwater medium acts as a natural low-pass filter on angular radiance. Scattering suppresses high-frequency view-dependent signals, making high-order SHs redundant. Moreover, our formulation explicitly embeds wavelength-dependent optical parameters into each Gaussian, allowing the model to explain spectral and view variations physically rather than through a purely expressive SH basis. As a result, relying on high-order SHs risks introducing redundant degrees of freedom that may interfere with parameter interpretability and overfit sparse views in underwater datasets. We conduct experiments under different

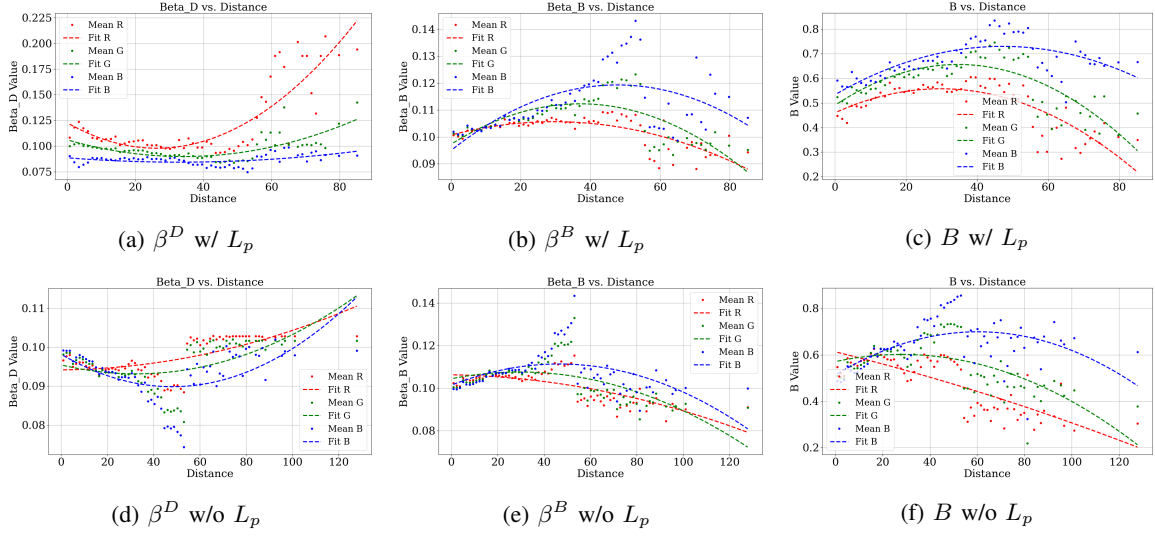


Fig. 5. Visualization of learned optical parameters with/without  $L_p$  on the IUI3-RedSea scene.

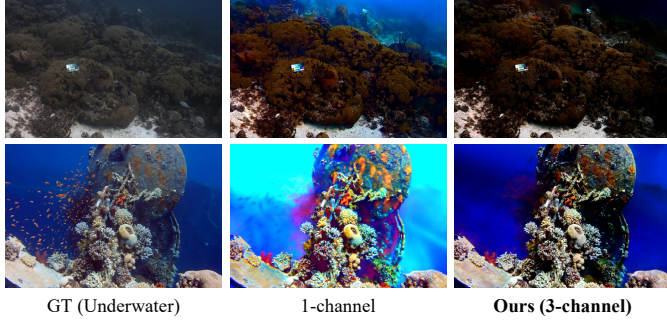


Fig. 6. Effect of single-channel vs. RGB-channel optical modeling.

SH degrees, as shown in Table V. Interestingly, lowering SH degree even slightly improves PSNR (+0.14). We attribute this to the reduced overfitting caused by excessive SH parameters and the improved stability of color estimation under our physically grounded formulation. Moreover, reducing the SH degree significantly decreases the overall model size: color parameters drop from 48 at degree-3 to 3 per Gaussian at degree-0, leading to a substantial savings in storage and computation. Even with comparable numbers of Gaussians (differs 1%), using degree-0 SH reduces memory consumption by  $\sim 63\%$  and improves rendering speed by  $\sim 20\%$ . We therefore adopt degree-0 (RGB only) in all experiments, achieving a favorable balance between accuracy, compactness, and real-time performance.

#### E. Ablation Study

To validate the effectiveness of each component in our proposed WaterClear-GS, we conduct a series of ablation studies on the SeaThru-NeRF dataset. As shown in Table VI, the full model achieves the best performance on both the NVS and UIR tasks, demonstrating the complementary benefits of all components.

1) *Effectiveness of the Depth-Guided Geometric Regularization:* Figure 7 and Table VII compare different forms of

TABLE V  
QUANTITATIVE RESULTS OF DIFFERENT SH DEGREE ON THE J.G-REDSEA SCENE. STORAGE IS BASED ON THE SIZE OF THE EXPORTED PLY FILE, WHICH IS RELATIVE TO THE NUMBER OF GAUSSIANS AND THE NUMBER OF ATTRIBUTE PARAMETERS PER GAUSSIAN. **BOLD** DENOTES THE BEST PERFORMANCE.

SH Degree	Gaussians(K)	Storage(MB)↓	PSNR↑	Time(min)↓	FPS↑
3	1528	414	24.21	17	127.58
2	1526	291	24.27	16	134.84
1	1542	206	24.31	15.5	144.71
<b>Ours (0)</b>	1540	<b>153</b>	<b>24.35</b>	<b>15</b>	<b>152.72</b>

TABLE VI  
ABLATION RESULTS ON THE SEATHRU-NERF DATASET. UIR METRICS ARE MEASURED ON CURASAO SCENE. **BOLD** DENOTES THE BEST PERFORMANCE, AND UNDERLINE DENOTES THE SECOND PLACE.

Method	NVS			UIR	
	PSNR↑	SSIM↑	LPIPS↓	$\triangle E_{00} \downarrow$	$\bar{\psi} \downarrow$
Baseline (3DGS)	26.71	0.901	0.204	-	-
w/o $L_d$	28.75	0.926	0.154	<u>12.93</u>	11.78
w/o weighted $L_{img}$	29.06	0.899	0.246	13.12	<u>11.09</u>
w/o $L_e$	29.84	0.930	0.151	15.61	14.69
w/o $L_s$	29.68	0.929	0.151	13.77	14.14
w/o $L_p$	<u>29.98</u>	<u>0.930</u>	<u>0.150</u>	15.56	15.48
<b>Ours (Full Model)</b>	<b>30.04</b>	<b>0.931</b>	<b>0.149</b>	<b>12.67</b>	<b>10.71</b>

depth regularization. Without using any depth prior, the reconstruction exhibits noticeable artifacts and floating noise, as the model lacks geometric guidance to suppress medium-induced ambiguities. Incorporating an L1 loss on depth provides partial improvement by encouraging coarse alignment. An L2 depth loss enforces overly strict pixel-wise matching, leading to severe 'holes' and discontinuities in the predicted depth due to the inevitable scale and shift inconsistencies present in monocular depth maps. In contrast, with our PCC-based depth regularization, the model achieves the highest reconstruction accuracy while producing smooth and geometrically coherent depth maps. We attribute this robustness to the scale- and shift-

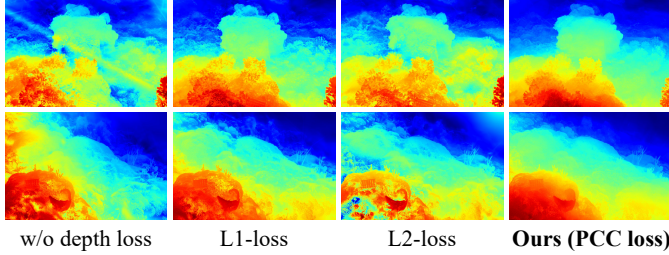


Fig. 7. **Visualization of depth maps under different depth loss functions.** The proposed PCC depth loss produces noticeably smoother and more spatially consistent depth estimates compared to alternative losses.

TABLE VII

RESULTS OF DIFFERENT  $L_d$  ON THE SEATHRU-NERF DATASET. **BOLD** DENOTES THE BEST PERFORMANCE.

Method	PSNR↑	SSIM↑	LPIPS↓
w/o depth loss	28.75	0.926	0.154
w L1	29.51	0.929	0.152
w L2	29.84	0.930	0.151
<b>Ours (PCC loss)</b>	<b>30.04</b>	<b>0.931</b>	<b>0.149</b>

TABLE VIII

RESULTS OF DIFFERENT  $L_{img}$  ON THE SEATHRU-NERF DATASET. **BOLD** DENOTES THE BEST PERFORMANCE, AND UNDERLINE DENOTES THE SECOND PLACE.

Method	PSNR↑	SSIM↑	LPIPS↓
L1+DSSIM	29.06	0.899	0.246
W-L1+DSSIM	29.34	0.918	0.184
L1+W-DSSIM	29.19	0.919	0.183
W-L1+W-DSSIM	<u>29.85</u>	<u>0.929</u>	<u>0.151</u>
L2+DSSIM	28.28	0.880	0.286
W-L2+DSSIM	29.14	0.903	0.237
L2+W-DSSIM	28.61	0.912	0.200
<b>Ours (W-L2+W-DSSIM)</b>	<b>30.04</b>	<b>0.931</b>	<b>0.149</b>

invariant nature of PCC, which makes it better suited for supervising monocular depth priors that may not be geometrically consistent with the reconstructed 3D scene.

2) *Effectiveness of the Perception-Driven Image Loss:* Figure 10 and Table VIII report the impact of different configurations of photometric and structural losses. Replacing standard L1, L2, and SSIM with our perception-driven variants (W-L1, W-L2, and W-DSSIM) consistently improves reconstruction quality. For example, W-L1+DSSIM increases PSNR from 29.06 to 29.34 and reduces LPIPS from 0.246 to 0.184, showing that inverse-intensity reweighting better supervises underexposed regions. Introducing W-DSSIM provides additional structural improvement (29.19 PSNR and 0.183 LPIPS). While standard L2 performs poorly (28.28 PSNR and 0.286 LPIPS), its weighted form greatly alleviates over-penalization of bright regions, achieving 29.14 PSNR and 0.237 LPIPS. The best performance is obtained by combining both weighted terms (W-L2+W-DSSIM), which reaches 30.04 PSNR, 0.931 SSIM, and 0.149 LPIPS. These results confirm that the proposed perception-driven transformation redistributes gradient emphasis toward underexposed regions and leads to noticeably improved reconstruction quality.

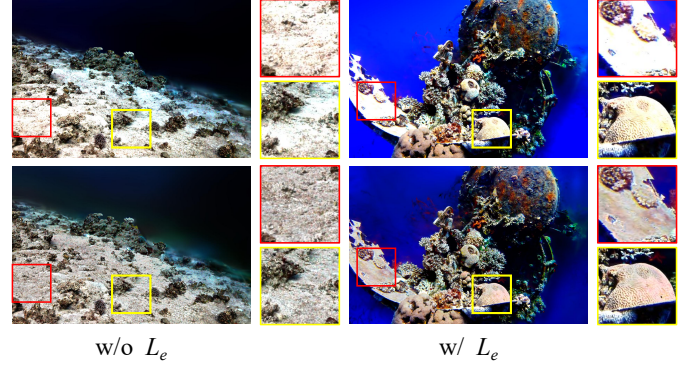


Fig. 8. **Visualization of the contribution of the exposure constraint.** With the introduction of  $L_e$ , the model effectively suppresses over-exposure and produces visually more natural and balanced restorations. Details are zoomed in and highlighted with red and yellow bounding boxes.

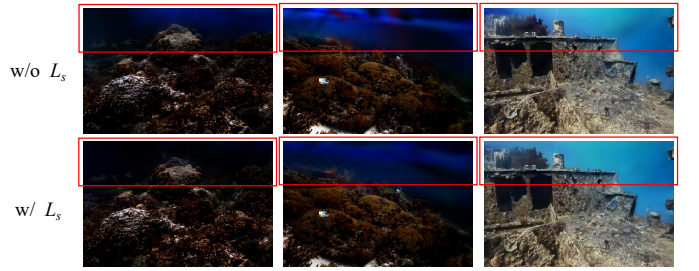


Fig. 9. **Visualization of the contribution of the spatial constraint.** With the introduction of  $L_s$ , the model produces restored results with fewer spatially inconsistent colors (highlighted with the red boxes).

3) *Effectiveness of the Exposure Constraint:* As shown in Figure 8, removing the exposure constraint leads to noticeable overexposure in bright or near-white regions. In scenes such as IUI3-RedSea and ShipWreck-1, objects with inherently high albedo produce strong highlights in the water-free rendering, causing unnatural colors and loss of fine texture. By imposing our exposure constraint, the model effectively suppresses such over-amplification, yielding more faithful color reproduction and preserving surface details. This demonstrates that the exposure constraint provides a useful regularization signal that prevents the network from overcompensating in highly illuminated regions and improves perceptual realism in the restored images.

4) *Effectiveness of the Spatially-Adaptive Regularization:* As evidenced by the visual results in Figure 9, removing spatial regularization leads to noticeable inconsistency in the estimated water-related parameters, represented as color discontinuities and local jumps in homogeneous background regions. Our spatially-adaptive regularization enforces coherence among neighboring Gaussians by encouraging smooth variations in the learned optical coefficients, which improves the overall visual continuity of the reconstructed scene. This produces more stable and spatially consistent color restoration, particularly in large water-body areas where the underlying medium properties should vary gradually.

5) *Effectiveness of the Physically Guided Spectral Regularization:* Figure 5 visualizes the learned optical parameters with and without applying the proposed physical prior.

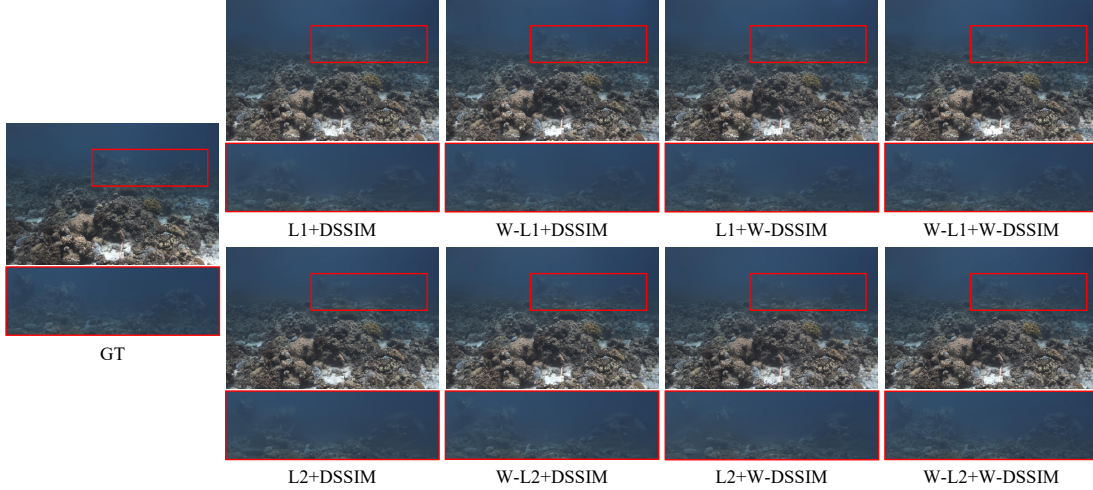


Fig. 10. Qualitative comparison of different image losses.

Without this regularization, the model is still able to capture coarse spectral tendencies, but the separation between RGB channels becomes weaker and violations of expected physical ordering occur frequently. This indicates that the raw data term alone is insufficient to reliably disambiguate the wavelength-dependent behavior of attenuation, scattering, and veiling light. By enforcing soft spectral ordering, our physical prior substantially stabilizes the optimization and yields optical parameter fields that are more consistent, interpretable, and aligned with underwater light-transport principles. This not only improves the physical plausibility of the learned parameters but also enhances the robustness of the reconstruction, demonstrating the effectiveness of incorporating physics-aware regularization into Gaussian-based modeling.

## V. CONCLUSION AND DISCUSSION

We presented WaterClear-GS, a purely Gaussian-based underwater reconstruction and restoration framework that embeds a physically grounded underwater formation model into 3D Gaussian primitives. By jointly learning wavelength-dependent attenuation, backscatter, and veiling light within the Gaussian representation, combined with geometric and optical regularization, our method achieves high-quality novel view synthesis and underwater image restoration while preserving the real-time rendering capability (160+ FPS).

Current limitations include handling only static scenes without addressing dynamic elements or temporal lighting variations. Meanwhile, both existing methods and ours struggle in extreme underwater environments, such as those with very high turbidity, which makes accurate color recovery exceedingly difficult. Improving performance in these challenging scenarios is a key objective for future research in this field.

## REFERENCES

- [1] L. Cai, N. E. McGuire, R. Hanlon, T. A. Mooney, and Y. Girdhar, “Semi-supervised visual tracking of marine animals using autonomous underwater vehicles,” *International Journal of Computer Vision*, vol. 131, no. 6, pp. 1406–1427, 2023. [1](#)
- [2] B. Joshi, M. Xanthidis, M. Roznere, N. J. Burgdorfer, P. Mordohai, A. Q. Li, and I. Rekleitis, “Underwater exploration and mapping,” in *2022 IEEE/OES Autonomous Underwater Vehicles Symposium (AUV)*. IEEE, 2022, pp. 1–7. [1](#)
- [3] E. Galceran, R. Campos, N. Palomeras, D. Ribas, M. Carreras, and P. Ridao, “Coverage path planning with real-time replanning and surface reconstruction for inspection of three-dimensional underwater structures using autonomous underwater vehicles,” *Journal of Field Robotics*, vol. 32, no. 7, pp. 952–983, 2015. [1](#)
- [4] J. J. Leonard and A. Bahr, “Autonomous underwater vehicle navigation,” *Springer handbook of ocean engineering*, pp. 341–358, 2016. [1](#)
- [5] M. Johnson-Roberson, M. Bryson, A. Friedman, O. Pizarro, G. Troni, P. Ozog, and J. C. Henderson, “High-resolution underwater robotic vision-based mapping and three-dimensional reconstruction for archaeology,” *Journal of Field Robotics*, vol. 34, no. 4, pp. 625–643, 2017. [1](#)
- [6] T. Missiaen, D. Sakellariou, and N. C. Flemming, “Survey strategies and techniques in underwater geoarchaeological research: An overview with emphasis on prehistoric sites,” *Under the sea: Archaeology and palaeolandscapes of the continental shelf*, pp. 21–37, 2017. [1](#)
- [7] Ancuti, Codruta, O and Ancuti, Cosmin and De Vleeschouwer, Christophe and Bekaert, Philippe, “Color balance and fusion for underwater image enhancement,” *IEEE Transactions on image processing*, vol. 27, no. 1, pp. 379–393, 2017. [1, 2](#)
- [8] C. O. Ancuti, C. Ancuti, C. De Vleeschouwer, and P. Bekaert, “Color balance and fusion for underwater image enhancement,” *IEEE Transactions on image processing*, vol. 27, no. 1, pp. 379–393, 2017. [1, 2](#)
- [9] Q. Qi, Y. Zhang, F. Tian, Q. M. J. Wu, K. Li, X. Luan, and D. Song, “Underwater image co-enhancement with correlation feature matching and joint learning,” *IEEE Transactions on Circuits and Systems for Video Technology*, vol. 32, no. 3, pp. 1133–1147, 2022. [1, 2](#)
- [10] Y. Kang, Q. Jiang, C. Li, W. Ren, H. Liu, and P. Wang, “A perception-aware decomposition and fusion framework for underwater image enhancement,” *IEEE Transactions on Circuits and Systems for Video Technology*, vol. 33, no. 3, pp. 988–1002, 2023. [1, 2](#)
- [11] G. Hou, N. Li, P. Zhuang, K. Li, H. Sun, and C. Li, “Non-uniform illumination underwater image restoration via illumination channel sparsity prior,” *IEEE Transactions on Circuits and Systems for Video Technology*, vol. 34, no. 2, pp. 799–814, 2024. [1, 2](#)
- [12] W. Zhang, L. Zhou, P. Zhuang, G. Li, X. Pan, W. Zhao, and C. Li, “Underwater image enhancement via weighted wavelet visual perception fusion,” *IEEE Transactions on Circuits and Systems for Video Technology*, vol. 34, no. 4, pp. 2469–2483, 2024. [1, 2](#)
- [13] B. Mildenhall, P. P. Srinivasan, M. Tancik, J. T. Barron, R. Ramamoorthi, and R. Ng, “Nerf: Representing scenes as neural radiance fields for view synthesis,” *Communications of the ACM*, vol. 65, no. 1, pp. 99–106, 2021. [1, 2](#)
- [14] D. Levy, A. Peleg, N. Pearl, D. Rosenbaum, D. Akkaynak, S. Korman, and T. Treibitz, “Seathru-nerf: Neural radiance fields in scattering

media,” in *Proceedings of the IEEE/CVF conference on computer vision and pattern recognition*, 2023, pp. 56–65. [1](#), [2](#), [5](#), [6](#), [9](#)

[15] T. Zhang and M. Johnson-Roberson, “Beyond nerf underwater: Learning neural reflectance fields for true color correction of marine imagery,” *IEEE Robotics and Automation Letters*, vol. 8, no. 10, pp. 6467–6474, 2023. [1](#), [2](#)

[16] Y. Tang, C. Zhu, R. Wan, C. Xu, and B. Shi, “Neural underwater scene representation,” in *Proceedings of the IEEE/CVF Conference on Computer Vision and Pattern Recognition*, 2024, pp. 11780–11789. [1](#), [2](#)

[17] B. Kerbl, G. Kopanas, T. Leimkühler, and G. Drettakis, “3d gaussian splatting for real-time radiance field rendering,” *ACM Trans. Graph.*, vol. 42, no. 4, pp. 139–1, 2023. [1](#), [2](#), [6](#)

[18] H. Li, W. Song, T. Xu, A. Elsig, and J. Kulhanek, “WaterSplatting: Fast underwater 3D scene reconstruction using gaussian splatting,” *3DV*, 2025. [1](#), [2](#), [6](#), [9](#)

[19] D. Yang, J. J. Leonard, and Y. Girdhar, “Seasplat: Representing underwater scenes with 3d gaussian splatting and a physically grounded image formation model,” *arXiv preprint arXiv:2409.17345*, 2024. [1](#), [2](#), [6](#), [9](#)

[20] S. Liu, J. Lu, Z. Gu, J. Li, and Y. Deng, “Aquatic-gs: A hybrid 3d representation for underwater scenes,” *arXiv preprint arXiv:2411.00239*, 2024. [1](#), [2](#)

[21] Y. Qiao, M. Shao, L. Meng, and K. Xu, “Restorgs: Depth-aware gaussian splatting for efficient 3d scene restoration,” in *Proceedings of the Computer Vision and Pattern Recognition Conference*, 2025, pp. 11177–11186. [1](#), [2](#)

[22] T. Müller, A. Evans, C. Schied, and A. Keller, “Instant neural graphics primitives with a multiresolution hash encoding,” *ACM transactions on graphics (TOG)*, vol. 41, no. 4, pp. 1–15, 2022. [2](#)

[23] A. Chen, Z. Xu, A. Geiger, J. Yu, and H. Su, “Tensorf: Tensorial radiance fields,” in *European conference on computer vision*. Springer, 2022, pp. 333–350. [2](#)

[24] S. Fridovich-Keil, A. Yu, M. Tancik, Q. Chen, B. Recht, and A. Kanazawa, “Plenoxels: Radiance fields without neural networks,” in *Proceedings of the IEEE/CVF conference on computer vision and pattern recognition*, 2022, pp. 5501–5510. [2](#)

[25] S. Fang, Y. Wang, Y. Yang, W. Xu, H. Wang, W. Ding, and S. Zhou, “Pvd-al: Progressive volume distillation with active learning for efficient conversion between different nerf architectures,” *arXiv preprint arXiv:2304.04012*, vol. 3, 2023. [2](#)

[26] S. Fang, W. Xu, H. Wang, Y. Yang, Y. Wang, and S. Zhou, “One is all: Bridging the gap between neural radiance fields architectures with progressive volume distillation,” in *Proceedings of the AAAI Conference on Artificial Intelligence*, vol. 37, no. 1, 2023, pp. 597–605. [2](#)

[27] S. Fang, D. Qi, W. Xu, Y. Wang, Z. Zhang, X. Zhang, H. Zhang, Z. Shao, and W. Ding, “Efficient implicit sdf and color reconstruction via shared feature field,” in *Proceedings of the Asian Conference on Computer Vision*, 2024, pp. 3499–3516. [2](#)

[28] X. Zhang, P. P. Srinivasan, B. Deng, P. Debevec, W. T. Freeman, and J. T. Barron, “Nerfactor: Neural factorization of shape and reflectance under an unknown illumination,” *ACM Transactions on Graphics (ToG)*, vol. 40, no. 6, pp. 1–18, 2021. [2](#)

[29] J. T. Barron, B. Mildenhall, M. Tancik, P. Hedman, R. Martin-Brualla, and P. P. Srinivasan, “Mip-nerf: A multiscale representation for anti-aliasing neural radiance fields,” in *Proceedings of the IEEE/CVF international conference on computer vision*, 2021, pp. 5855–5864. [2](#)

[30] Y. Wang, S. Fang, H. Zhang, H. Li, Z. Zhang, X. Zeng, and W. Ding, “Uav-enerf: Text-driven uav scene editing with neural radiance fields,” *IEEE Transactions on Geoscience and Remote Sensing*, vol. 62, pp. 1–14, 2024. [2](#)

[31] K. Zhang, G. Riegler, N. Snavely, and V. Koltun, “Nerf++: Analyzing and improving neural radiance fields,” *arXiv preprint arXiv:2010.07492*, 2020. [2](#)

[32] S. Fridovich-Keil, G. Meanti, F. R. Warburg, B. Recht, and A. Kanazawa, “K-planes: Explicit radiance fields in space, time, and appearance,” in *Proceedings of the IEEE/CVF Conference on Computer Vision and Pattern Recognition (CVPR)*, June 2023, pp. 12479–12488. [2](#)

[33] A. Pumarola, E. Corona, G. Pons-Moll, and F. Moreno-Noguer, “D-nerf: Neural radiance fields for dynamic scenes,” in *Proceedings of the IEEE/CVF conference on computer vision and pattern recognition*, 2021, pp. 10318–10327. [2](#)

[34] K. Park, U. Sinha, P. Hedman, J. T. Barron, S. Bouaziz, D. B. Goldman, R. Martin-Brualla, and S. M. Seitz, “Hypernerf: A higher-dimensional representation for topologically varying neural radiance fields,” *ACM Trans. Graph.*, vol. 40, no. 6, dec 2021. [2](#)

[35] A. Lin, Y. Xiang, J. Li, and M. Prasad, “Dynamic appearance particle neural radiance field,” *IEEE Transactions on Circuits and Systems for Video Technology*, 2025. [2](#)

[36] M. Tancik, V. Casser, X. Yan, S. Pradhan, B. Mildenhall, P. P. Srinivasan, J. T. Barron, and H. Kretzschmar, “Block-nerf: Scalable large scene neural view synthesis,” in *Proceedings of the IEEE/CVF conference on computer vision and pattern recognition*, 2022, pp. 8248–8258. [2](#)

[37] H. Turki, D. Ramanan, and M. Satyanarayanan, “Mega-nerf: Scalable construction of large-scale nerfs for virtual fly-throughs,” in *Proceedings of the IEEE/CVF conference on computer vision and pattern recognition*, 2022, pp. 12922–12931. [2](#)

[38] J. Li, J. Zhang, X. Bai, J. Zheng, X. Ning, J. Zhou, and L. Gu, “Dngaussian: Optimizing sparse-view 3d gaussian radiance fields with global-local depth normalization,” in *Proceedings of the IEEE/CVF conference on computer vision and pattern recognition*, 2024, pp. 20775–20785. [2](#)

[39] Y. Chen, H. Xu, C. Zheng, B. Zhuang, M. Pollefeys, A. Geiger, T.-J. Cham, and J. Cai, “Mvsplat: Efficient 3d gaussian splatting from sparse multi-view images,” in *European Conference on Computer Vision*. Springer, 2024, pp. 370–386. [2](#)

[40] Y. Niu, X. Li, and Y. Wang, “Stereo-gaussian: Enhanced sparse view gaussian splatting with one stereopair for light-field 3d display,” *IEEE Transactions on Circuits and Systems for Video Technology*, pp. 1–1, 2025. [2](#)

[41] S. Fang, I. Shen, T. Igarashi, Y. Wang, Z. Wang, Y. Yang, W. Ding, S. Zhou *et al.*, “Nerf is a valuable assistant for 3d gaussian splatting,” in *Proceedings of the IEEE/CVF International Conference on Computer Vision*, 2025, pp. 26230–26240. [2](#)

[42] Y. Lin, Z. Dai, S. Zhu, and Y. Yao, “Gaussian-flow: 4d reconstruction with dynamic 3d gaussian particle,” in *Proceedings of the IEEE/CVF Conference on Computer Vision and Pattern Recognition*, 2024, pp. 21136–21145. [2](#)

[43] J. Sun, H. Jiao, G. Li, Z. Zhang, L. Zhao, and W. Xing, “3dgstream: On-the-fly training of 3d gaussians for efficient streaming of photo-realistic free-viewpoint videos,” in *Proceedings of the IEEE/CVF Conference on Computer Vision and Pattern Recognition*, 2024, pp. 20675–20685. [2](#)

[44] J. Lin, Z. Li, X. Tang, J. Liu, S. Liu, J. Liu, Y. Lu, X. Wu, S. Xu, Y. Yan *et al.*, “Vastgaussian: Vast 3d gaussians for large scene reconstruction,” in *Proceedings of the IEEE/CVF Conference on Computer Vision and Pattern Recognition*, 2024, pp. 5166–5175. [2](#)

[45] J. Chen, W. Ye, Y. Wang, D. Chen, D. Huang, W. Ouyang, G. Zhang, Y. Qiao, and T. He, “Gigags: Scaling up planar-based 3d gaussians for large scene surface reconstruction,” *arXiv preprint arXiv:2409.06685*, 2024. [2](#)

[46] Y. Liu, C. Luo, L. Fan, N. Wang, J. Peng, and Z. Zhang, “Citygaussian: Real-time high-quality large-scale scene rendering with gaussians,” in *European Conference on Computer Vision*. Springer, 2024, pp. 265–282. [2](#)

[47] X. Cui, W. Ye, Y. Wang, G. Zhang, W. Zhou, T. He, and H. Li, “Streetsurfsgs: Scalable urban street surface reconstruction with planar-based gaussian splatting,” *IEEE Transactions on Circuits and Systems for Video Technology*, vol. 35, no. 9, pp. 8780–8793, 2025. [2](#)

[48] J. Gao, C. Gu, Y. Lin, H. Zhu, X. Cao, L. Zhang, and Y. Yao, “Relightable 3d gaussian: Real-time point cloud relighting with brdf decomposition and ray tracing,” *arXiv:2311.16043*, 2023. [2](#)

[49] Y. Jiang, J. Tu, Y. Liu, X. Gao, X. Long, W. Wang, and Y. Ma, “Gaussianshader: 3d gaussian splatting with shading functions for reflective surfaces,” *arXiv preprint arXiv:2311.17977*, 2023. [2](#)

[50] Z. Liu, J. Su, G. Cai, Y. Chen, B. Zeng, and Z. Wang, “Georgs: Geometric regularization for real-time novel view synthesis from sparse inputs,” *IEEE Transactions on Circuits and Systems for Video Technology*, vol. 34, no. 12, pp. 13113–13126, 2024. [2](#)

[51] L. Fan, Y. Yang, M. Li, H. Li, and Z. Zhang, “Trim 3d gaussian splatting for accurate geometry representation,” *arXiv preprint arXiv:2406.07499*, 2024. [2](#)

[52] K. He, J. Sun, and X. Tang, “Single image haze removal using dark channel prior,” *IEEE transactions on pattern analysis and machine intelligence*, vol. 33, no. 12, pp. 2341–2353, 2010. [2](#)

[53] N. Carlevaris-Bianco, A. Mohan, and R. M. Eustice, “Initial results in underwater single image dehazing,” in *Oceans 2010 Mts/IEEE Seattle*. IEEE, 2010, pp. 1–8. [2](#)

[54] D. Akkaynak and T. Treibitz, “A revised underwater image formation model,” in *Proceedings of the IEEE conference on computer vision and pattern recognition*, 2018, pp. 6723–6732. [2](#), [3](#)

[55] J. Xie, G. Hou, G. Wang, and Z. Pan, “A variational framework for underwater image dehazing and deblurring,” *IEEE Transactions on Circuits and Systems for Video Technology*, vol. 32, no. 6, pp. 3514–3526, 2022. [2](#)

- [56] A. V. Sethuraman, M. S. Ramanagopal, and K. A. Skinner, "Waternerf: Neural radiance fields for underwater scenes," in *OCEANS 2023-MTS/IEEE US Gulf Coast*. IEEE, 2023, pp. 1–7. [2](#)
- [57] J. Zhou, T. Liang, D. Zhang, S. Liu, J. Wang, and E. Q. Wu, "Waterhenerf: Water-ray matching neural radiance fields for underwater scene reconstruction," *Information Fusion*, vol. 115, p. 102770, 2025. [2](#)
- [58] Y. Bekerman, S. Avidan, and T. Treibitz, "Unveiling optical properties in underwater images," in *2020 IEEE International Conference on Computational Photography (ICCP)*. IEEE, 2020, pp. 1–12. [3](#), [6](#)
- [59] L. Yang, B. Kang, Z. Huang, Z. Zhao, X. Xu, J. Feng, and H. Zhao, "Depth anything v2," *arXiv:2406.09414*, 2024. [4](#)
- [60] B. Mildenhall, P. Hedman, R. Martin-Brualla, P. P. Srinivasan, and J. T. Barron, "Nerf in the dark: High dynamic range view synthesis from noisy raw images," in *Proceedings of the IEEE/CVF Conference on Computer Vision and Pattern Recognition (CVPR)*, June 2022, pp. 16 190–16 199. [4](#)
- [61] D. Akkaynak and T. Treibitz, "Sea-thru: A method for removing water from underwater images," in *Proceedings of the IEEE/CVF conference on computer vision and pattern recognition*, 2019, pp. 1682–1691. [5](#)
- [62] J. L. Schonberger and J.-M. Frahm, "Structure-from-motion revisited," in *Proceedings of the IEEE conference on computer vision and pattern recognition*, 2016, pp. 4104–4113. [5](#)
- [63] Z. Wang, A. C. Bovik, H. R. Sheikh, and E. P. Simoncelli, "Image quality assessment: from error visibility to structural similarity," *IEEE transactions on image processing*, vol. 13, no. 4, pp. 600–612, 2004. [6](#)
- [64] R. Zhang, P. Isola, A. A. Efros, E. Shechtman, and O. Wang, "The unreasonable effectiveness of deep features as a perceptual metric," in *Proceedings of the IEEE conference on computer vision and pattern recognition*, 2018, pp. 586–595. [6](#)
- [65] Z. Wang, L. Shen, M. Xu, M. Yu, K. Wang, and Y. Lin, "Domain adaptation for underwater image enhancement," *IEEE Transactions on Image Processing*, vol. 32, pp. 1442–1457, 2023. [6](#)
- [66] L. Peng, C. Zhu, and L. Bian, "U-shape transformer for underwater image enhancement," *IEEE transactions on image processing*, vol. 32, pp. 3066–3079, 2023. [6](#)
- [67] G. Sharma, W. Wu, and E. N. Dalal, "The ciede2000 color-difference formula: Implementation notes, supplementary test data, and mathematical observations," *Color Research & Application: Endorsed by Inter-Society Color Council, The Colour Group (Great Britain), Canadian Society for Color, Color Science Association of Japan, Dutch Society for the Study of Color, The Swedish Colour Centre Foundation, Colour Society of Australia, Centre Français de la Couleur*, vol. 30, no. 1, pp. 21–30, 2005. [6](#)
- [68] C. Boittiaux, R. Marxer, C. Dune, A. Arnaubec, M. Ferrera, and V. Hugel, "Sucré: Leveraging scene structure for underwater color restoration," in *2024 International Conference on 3D Vision (3DV)*. IEEE, 2024, pp. 1488–1497. [6](#)